Room Temperature Dynamic Strain Aging in Ultrafine-Grained Titanium

ARTICLE *in* METALLURGICAL AND MATERIALS TRANSACTIONS A · JULY 2015

Impact Factor: 1.73 · DOI: 10.1007/s11661-015-3061-7

Room Temperature Dynamic Strain Aging in Ultrafine-Grained Titanium

FELIPE PERISSÉ D. LOPES, CHIA HUI LU, SHITENG ZHAO, SERGIO N. MONTEIRO, and MARC A. MEYERS

Dynamic strain aging (DSA) in coarse-grained (CG) titanium is usually observed at intermediate to high temperatures 473 K to 973 K (200 °C to 700 °C) and is characterized by serrations in the stress *vs* strain curves. In the present work, despite the absence of apparent serrations, ultrafine-grained titanium (UFG Ti) undergoes DSA at room temperature, exhibited through an abnormal increase in the elastic limit and negative strain rate sensitivity. This effect is observed at 293 K (20 °C) in the strain rate interval of 10^{-4} to 10^{-2} s^{-1}, and at 203 K (−70 °C) and 373 K (100 °C) in a distinct strain rate range. Based on a calculated activation energy of 17.3 kJ/mol and microstructural observations by transmission electron microscopy, it is proposed that the dominant mechanism for DSA in UFG Ti involves interstitial solutes interacting with dislocations emitted from grain boundaries. The interstitials migrate from the grain boundaries along dislocation lines bowing out as they are emitted from the boundaries, a mechanism with a low calculated activation energy which is comparable with the experimental measurements. The dislocation velocities and interstitial diffusion along the dislocation cores are consistent.

DOI: 10.1007/s11661-015-3061-7

I. INTRODUCTION

THE yield point phenomenon was reported in titanium as early as 1953[1,2] and since then has been extensively investigated in various grades with grain sizes varying from 1 to 25 μm.[3–26] In addition to the observation of yield point and Lüders band formation caused by static strain aging, other responses which can be ascribed to dynamic strain aging (DSA) include serrations in the flow curve (Portevin-Le Châtelier effect), enhancement of the work hardening rate, humps in the temperature dependence of yield strength, reduction in ductility (blue brittleness effect), and abnormally low strain rate sensitivity.[7–15,18,22–26] Strong DSA effects in coarse-grained titanium extend from as low as 473 K to 973 K (200 °C to 700 °C). Most results were obtained for commercial purity grades with 2000 ppm of interstitial solutes.[9,12,18,22] However, even in high-purity Ti containing only 150 ppm of interstitials, DSA still occurs (although drastically reduced).[12] An activation energy of 172 kJ/mol for the onset of serrations in CG Ti[12] was found to be close to that for C and N lattice diffusion. This corroborates the mechanisms of dislocation pinning or dragging by interstitials (Cottrell atmosphere).[13,18,22]

In recent years, investigations on the mechanical behavior of ultrafine-grained titanium (UFG Ti) processed by severe plastic deformation (SPD) have received considerable attention due to its potential applications, primarily in the biomedical field. However, these studies have either ignored[27–41] or merely superficially discussed[42–44] the possible occurrence of DSA. Serrations in stress–strain curves were never analyzed in the UFG Ti processed by equal channel angular pressing (ECAP)[27,28,31–33,35,36,38–41] or equal channel angular extrusion (ECAE),[34,37] even though they were observed. Some room temperature (RT) tensile stress–strain curves for UFG Ti processed by high pressure torsion (HPT)[29,30] display a serrated plastic flow.

Blum and Breutinger[42] investigated the deformation kinetics of ECAPed UFG Ti and attributed a work softening at 723 K (450 °C) to DSA. Wang *et al.*[43] also discussed the possibility of DSA in ECAPed UFG Ti compressed at RT at quasi-static (10^{-4} to 10^{-1} s^{-1}) and dynamic (10^{3} to 10^{4} s^{-1}) strain rates. Stress–strain curves depicted by Wang *et al.*[43] reveal a jerky flow, which was not mentioned by the authors. Moreover, they report an abnormal strain hardening behavior at large strains and dynamic strain rates. Contrary to Blum and Breutinger,[42] Wang *et al.*[43] concluded that such behavior might be associated with twinning instead of DSA, despite little evidence of twinning activity reported at quasi-static strain rates except at very large strains.

Liu *et al.*[44] suggested the existence of DSA in ECAPed UFG Ti on the basis of serrations observed at 673 K (400 °C) and strain rate of 10^{-4} s^{-1}. Under these conditions, they reported a relatively high strain rate sensitivity of 0.1125, calculated by means of strain rate change tests.

FELIPE PERISSÉ D. LOPES, Graduate Student, and SERGIO N. MONTEIRO, Professor, are with the Materials Science Department, Military Institute of Engineering, IME, Rio de Janeiro Brazil. CHIA HUI LU, Graduate Student, SHITENG ZHAO, PhD Student, and MARC A. MEYERS, Distinguished Professor, are with the University of California, San Diego, CA. Contact e-mail: mameyers@eng.ucsd.edu

Manuscript submitted January 22, 2015.
Article published online July 24, 2015

As aforementioned, in coarse-grained (CG) Ti, one of the typical DSA effects is an abnormally low strain rate sensitivity,[8,9] which is contrary to the Liu *et al.*[44] findings. These authors also reported, without indicating the calculation method, an average activation energy of 104.46 kJ/mol in the temperature range from 298 K (25 °C) to 673 K (400 °C). By comparing this value with activation energies in the literature, Liu *et al.*[44] concluded that UFG Ti deformation is controlled by the grain boundaries in addition to dislocation slip and twinning. Transmission electron microscopy observations revealed a high dislocation density on UFG Ti compression tested at RT and strain rate of 10^{-3} s^{-1}.

Monteiro *et al.*[45] recently reported an anomalous strain rate effect in the range of 10^{-5} to 10^{-1} s^{-1} for RT tensile-tested UFG Ti processed by ECAP-Conform. A maximum in the ultimate strength was observed at a strain rate of 10^{-3} s^{-1}. This maximum in strength resulted in a negative strain rate sensitivity in the range of 10^{-3} to 10^{-1} s^{-1}.

The abnormal work hardening rate[43] and anomalous strain rate sensitivity[45] observed in UFG Ti motivated a deeper investigation in the temperature interval from 77 K to 473 K (−196 °C to 200 °C) at strain rates from 10^{-5} to 10^{-1} s^{-1}. The particular interest in ambient temperature is because UFG Ti processed by SPD is currently being considered for dental and biomedical applications owing to excellent biocompatibility as well as corrosion resistance and exceptional strength.[41,46–52]

II. EXPERIMENTAL PROCEDURE

The UFG Ti investigated in the present work was received as 300-mm-long and 6-mm-diameter rods processed by the ECAP-Conform technique.[53,54] The chemical composition determination was commissioned to the Evans Analytical Group (EAG), and the results are shown in Table I along with specifications for the different grades of commercially purity titanium as well as the Ti-6Al-4V alloy.[55]

Table I shows that the investigated UFG Ti, with the exception of oxygen, has comparatively lower amounts of Fe and interstitials. In particular, no hydrogen was detected by the IGF-TC method[56] according to the EAG report. In spite of lower impurity contents, the investigated UFG Ti is within the composition range of commercial purity, but not of the high-purity-level titanium.

Cylindrical compression specimens 4.75 mm in diameter and 4.75 mm in length were machined from the as-received rod. Special care was taken to ensure flat and parallel specimen circular end surfaces for compression tests. They were polished with emery paper followed by diamond paste. Compression tests were performed in a model 3367 Instron machine operating at temperatures from 77 K to 473 K (−196 °C to 200 °C), and strain rates from 10^{-5} to 10^{-1} s^{-1}. Before testing, the specimen end surfaces and the machine-connected compression plates were lubricated with an inorganic grease to minimize friction effects. A minimum of 3 specimens were used for each combination of temperature and strain rate. The yield stress was measured by drawing a line parallel to the elastic region of the stress–strain curves at an offset strain of 0.2 pct and obtaining the intersection point.

The microstructure of both as-received and deformed specimens was observed by TEM using a model Tecnai G2 Polara FEI electron microscope operating at 300 kV. Thin foil samples were initially cut in an Accutom 2 Struers saw, followed by a sequence of manual polishing (using abrasive papers and 0.05 μm alumina paste) and electro-polishing (using a 5 pct perchloric acid 35 pct butanol and 60 pct methanol mixture in a model Electropol 2 Struers device operating with 30 V to perforation), as per standard practice.[57]

III. RESULTS AND DISCUSSION

The grain size of the as-received UFG Ti is around 130 nm in TEM sections transverse to the axial direction of the rod (also the compression specimens' axis). However, grains as small as 20 nm were observed. After compression testing, elongated grains with lengths of 400 nm were detected and are associated with a rotation mechanism taking place during plastic deformation. These features are shown in detail along with TEM results and discussion in Section III–D.

A. *Compression Tests*

DSA effects in the same UFG Ti associated with a strength peak and negative strain rate sensitivity were observed in tensile tests at 293 K (20 °C) in the strain rate interval of 10^{-5} to 10^{-1} s^{-1}.[45] Hence, the present compression tests were conducted in this same strain rate interval at 77 K, 203 K, 293 K, 373 K, and 473 K (−196 °C, −70 °C, 20 °C, 100 °C, and 200 °C). Figure 1 illustrates typical stress–strain curves obtained at 20 °C for different strain rates. Only minor serrations are observed in Figure 1 (principally, at 10^{-4} s^{-1}). These

Table I. Chemical Composition (wt pct—Balance Ti) of Conventional Commercial Purity (CP)-Ti and Ti-6Al-4V alloy (Adapted from ASTM B348-11) as well as the investigated UFG Ti

Material	Grade	C	N	H	O	Fe
CP-Ti	1	0.080	0.030	0.0015	0.18	0.200
CP-Ti	2	0.080	0.030	0.0015	0.25	0.300
CP-Ti	3	0.080	0.050	0.0015	0.35	0.300
CP-Ti	4	0.080	0.050	0.0015	0.40	0.500
Ti-6Al-4V	5	0.080	0.050	0.0015	0.20	0.400
CP-Ti	UFG	0.043	0.006	—	0.33	0.016

serrations are consistent with the ones reported by Min *et al.*[58] for Mg ZEK 100 alloy.

Similar to previous reports on UFG Ti by Wang *et al.*,[43] the curves in Figure 1 exhibit little initial hardening. An enhanced work hardening rate is an effect attributed to DSA.[9,12,59] One is therefore inclined to disregard low-temperature DSA in UFG Ti. However, the plot of yield stress *vs* the logarithm of the strain rate in Figure 2 reveals a stress hump in the range of 10^{-4} to 10^{-2} s^{-1}. In the temperature range from 77 K to 473 K (−196 °C to 200 °C), shown in (Figure 2(a)), the yield stress increases monotonically with strain rate without a hump. For 203 K, 293 K, and 373 K (−70 °C, 20 °C, and 100 °C), humps are unequivocally present. This anomalous increase in stress is magnified in (Figure 2(b)). Considering the statistical precision of the error bars (standard deviation), the hump for the 293 K (20 °C) curve stands almost 100 MPa above the base (dashed) line at the center of the interval, 3×10^{-3} s^{-1}. Although not as prominent, the humps at 203 K and 373 K (−70 °C and 100 °C), with base line increments up to 60 MPa for 10^{-4} s^{-1} and 30 MPa for 10^{-2} s^{-1}, respectively, are statistically reliable.

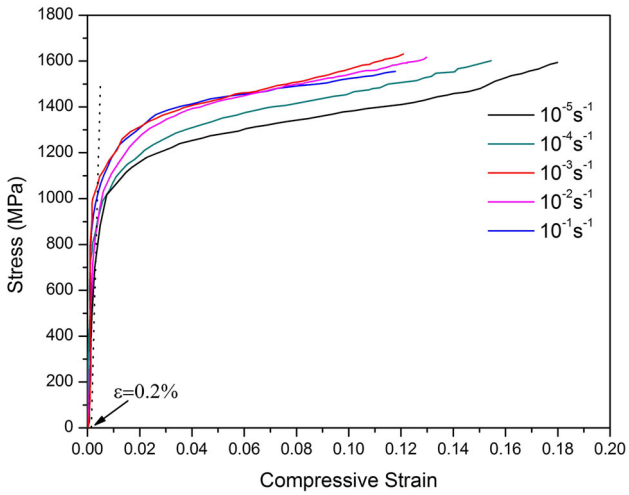

Fig. 1—Typical room temperature compressive stress–strain curves UFG Ti at different strain rates. The same effect was observed in previous tensile tests conducted by Monteiro *et al.*[45]: 10^{-5} s^{-1}: $\sigma_y = 762 \pm 23$ MPa; 10^{-3} s^{-1}: $\sigma_y = 892 \pm 14$ MPa; $10^{-1} s^{-1}$: $\sigma_y = 855 \pm 20$ MPa.

B. *Strain Rate Sensitivity and Activation Volume*

Abnormally low or even negative strain rate sensitivity $m = d\ln\sigma/d\ln\dot{\varepsilon}$ is associated with stress humps in metals showing DSA.[18,22,59] Figure 2 depicts stress *vs* strain rate curves showing negative strain rate sensitivity at 293 K (20 °C) from 10^{-3} to 10^{-2} s^{-1} ($m = -0.017$), and at 203 K (−70 °C) from 10^{-4} to 10^{-3} s^{-1} ($m = -0.022$). Depending on the strain rate interval, higher values of strain rate sensitivity may also be found; $m = 0.10$ at 293 K (20 °C) from 10^{-4} to 3×10^{-4} s^{-1} due to the "bell-shaped" hump. This could be a cause of the higher value of strain rate sensitivity in association with DSA reported by Liu *et al.*[44]

Thermally activated stress-enabled dislocation motion is represented by the classic Arrhenius expression for the shear strain rate (Seeger[59]):

$$\dot{\gamma} = \dot{\gamma}_0 \exp\left(-\frac{\Delta G_0 - \tau V}{kT}\right), \qquad [1]$$

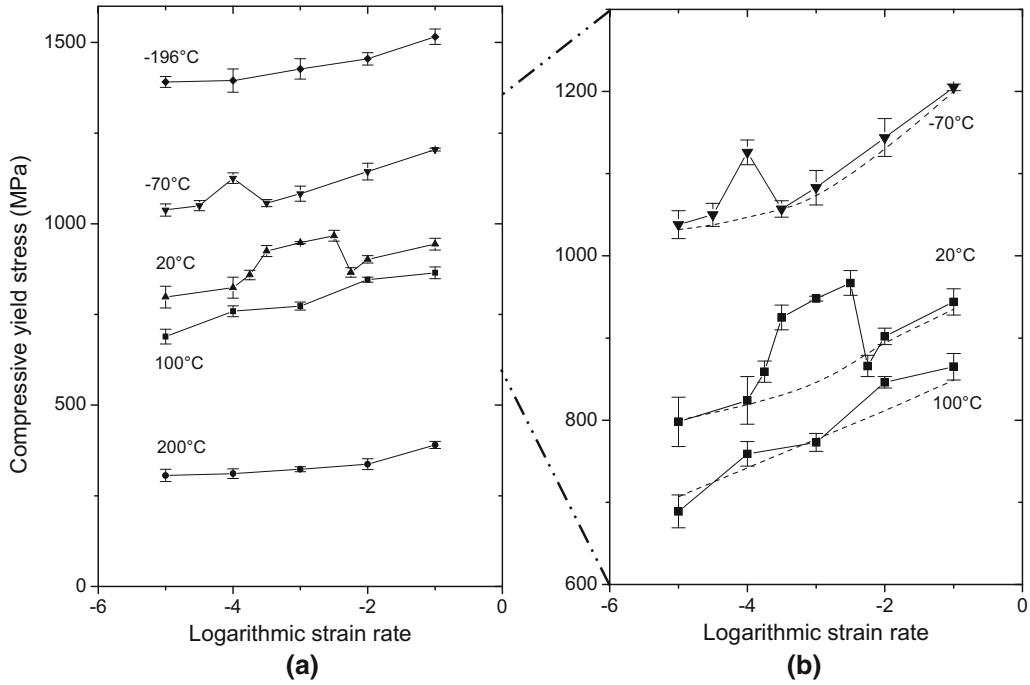

Fig. 2—Strain rate dependence of the yield stress for UFG Ti compression tested with temperatures ranging from 77 K (−196) to 473 K (200 °C): general curves (*a*) and magnified curves evidencing DSA humps (*b*).

where ΔG_0, τ, k, and T are zero temperature activation energy of plastic deformation, effective shear stress on dislocation, Boltzmann constant, and absolute temperature, respectively. The activation volume is a measure of the volume of obstacle encountered by a dislocation, equal to the product of the activation area A (the area swept by a dislocation between obstacles) and the Burgers vector, b (b = 0.289 nm): V = Ab Taking the logarithm on both sides of Eq. [1],

$$\ln \dot{\gamma} = \ln \dot{\gamma}_0 - \frac{\Delta G_0}{kT} + \frac{\tau V}{kT} = \frac{\tau V}{kT} + C \qquad [2]$$

where C is a constant at a fixed temperature T. Differentiating both sides with respect to the effective stress at constant T:

$$V = kT\left(\frac{\partial \ln \dot{\gamma}}{\partial \tau}\right)_T = \frac{kT}{\tau}\left(\frac{\partial \ln \dot{\gamma}}{\partial \ln \tau}\right)_T \qquad [3]$$

Noting that $\frac{\partial \ln \dot{\gamma}}{\partial \ln \tau}$ is the reciprocal of strain rate sensitivity, and that τ can roughly be related to the yield strength, $\sigma_y = \sqrt{3}\tau$ (by von Mises criterion) Eq. [3] can be rewritten as

$$V = \sqrt{3}\frac{kT}{m\sigma_y} \qquad [4]$$

As determined in Figure 2, the strain rate sensitivity of UFG Ti at RT 293 K (20 °C) is $m \sim 0.10$ in the interval from 10^{-4} to 10^{-3} s^{-1}. Therefore, the corresponding activation volume can be calculated as $V \sim 3b^3$, where b is the Burgers vector in hexagonal titanium. Such a small activation volume, compared with $80b^3$ for CG Ti,[4] suggests that plastic deformation is controlled by barriers with a small volume, and therefore, DSA should occur in a localized manner. Grain boundaries in SPD-fabricated UFG materials are known for their non-equilibrium nature.[60] In these nanostructured materials, a large concentration of dislocations is found in the vicinity of grain boundaries, which may be susceptible to DSA.

C. *Activation Energy for Dynamic Strain Aging*

In principle, no phenomenon except DSA can be responsible for the stress humps and negative strain rate sensitivity shown in Figure 2. The DSA phenomenon exhibited by UFG Ti at low temperatures must be explained by some mechanism. In the case of serrated flow, the mechanism could be determined by the initial appearance of this particular effect. Indeed, Cottrell[61] first demonstrated that the onset of serrations in mild steel can be represented by an Arrhenius relationship between the strain rate ($\dot{\varepsilon}$) and the absolute temperature T:

$$\dot{\varepsilon} = A\exp(-\frac{Q}{RT}), \qquad [5]$$

where A is a pre-exponential term and Q the activation energy, which is related to the diffusion of interstitials. On a thermodynamic basis, Eq. [5] is equivalent to Eq. [1].

As aforementioned, Garde *et al.*[12] used Eq. [5] to find the value of Q for both the onset of serrations (172 kJ/mol) and the strain rate-dependent work hardening rate peak (247 kJ/mol) in commercial pure CG Ti. Work hardening rate peak is a normalized expression for the work hardening and is defined as $(\Delta\sigma/\Delta\varepsilon)(1/E)$. The present UFG Ti compression stress–strain curves at low temperatures, Figure 1, show only minor serrations and no evidence of work hardening rate peaks. This is attributed, as explained later, to the fact that this new mechanism of DSA operates only at the onset of plastic deformation.

If DSA is the controlling phenomenon, the temperatures at the maximum yield stress values in the humps, Figure 2, will have an Arrhenius strain rate dependence, Eq. [5]. Figure 3 shows the plot of $\ln \dot{\varepsilon}$ *vs* $1/T$ for values associated with the maximum yield stress in the humps of Figure 2. An approximate linear fit for the three points in Figure 3 yields an activation energy of 17.3 kJ/mol. This value is much lower than the activation energies associated with DSA in CG Ti.[12] Moreover, in terms of a possible contribution of interstitial atoms forming a dragging or pinning atmosphere for dislocations, there is no referenced Q value that can match the presently calculated one. In a review article on the effect of interstitial solutes, Conrad[22] presented activation energies for the bulk diffusion of oxygen, nitrogen, carbon, and hydrogen in different grades of α-Ti. Table II lists some of these activation energies.

Table II shows that the activation energies for interstitial bulk diffusion, even for the fastest hydrogen atoms, are significantly larger than the activation energy presently found for the low-temperature DSA in UFG Ti (17.3 kJ/mol). This discrepancy is reported here for the first time, since other works of DSA in UFG Ti[42,44] did not indicate activation energies.

D. *Non-Uniform Distribution of Dislocations in UFG Ti*

The very low activation energy suggests a smaller thermally activated barrier for the occurrence of DSA in UFG Ti, differing from the conventional mechanisms of DSA in Ti,[13,18,22] which occur through dislocation interaction, either by dragging or pinning, with a cloud

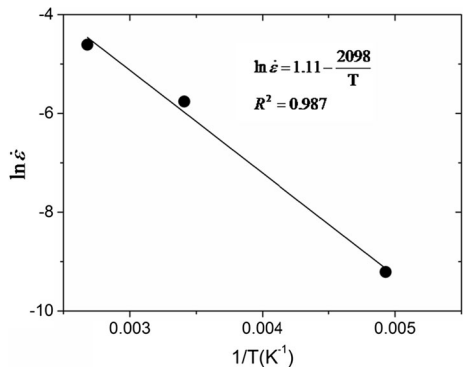

Fig. 3—Arrhenius plot for the strain rate dependence of maximum stress in UFG Ti compression tested at three temperatures: 203 K, 293 K, and 373 K (−70 °C, 20 °C, and 100 °C).

Table II. Activation Energies for Interstitial Atoms Volume Diffusion in α-Ti Lattice

Interstitial Element	O	N	C	H
Activation Energy (kJ/mol)	149 to 246	177 to 285	182 to 203	46 to 64

Adapted from Ref.[22].

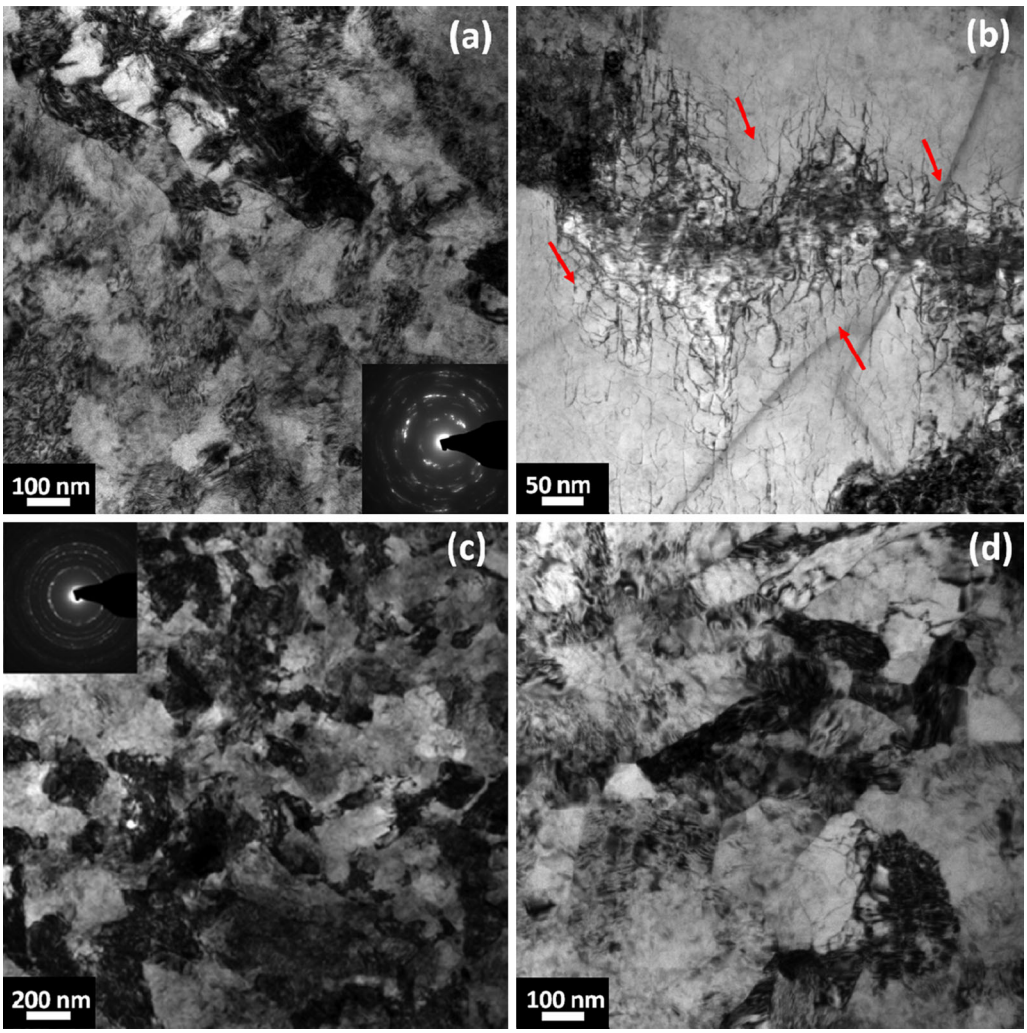

Fig. 4—Cross-sectional TEM shows the microstructure of (*a*) the as-ECAPed UFG Ti rod, and (*b*) its higher magnification, showing dislocations emitted from grain boundaries (marked by red arrow); (*c*) RT-compressed UFG Ti at 10^{-3} s^{-1} and (*d*) RT-compressed UFG Ti at 10^{-1} s^{-1}, both showing coalescence of nanocrystalline materials.

of solute atoms. Even the lowest Q value for hydrogen diffusion (46 kJ/mol, from Table II), an element not detected in the investigated UFG Ti (composition in Table I), is higher than the current value of 17.3 kJ/mol. The unique microstructure of UFG Ti must be the cause of the low Q value. Indeed, several works investigating the microstructure of ECAPed UFG Ti report sub micrometer grain sizes and high dislocation densities.[27,30,31,33,34,36,37,40,41] An estimated density of 10^{14} m^{-2} was calculated by Valiev *et al.*[30] A non-uniform distribution of dislocations that tend to accumulate and tangle around grain boundaries was also observed in ECAPed UFG Ti.[35,39,62] This was confirmed in the current investigation, as shown by the TEM image in Figure 4.

The cross-sectional TEM of the as-received ECAPed rod reveals a broad size distribution and many grains of irregular shape, as illustrated in Figure 4(a). The microstructure and the diffraction pattern with partial rings is a characteristic of ultrafine and nanostructured grains and subgrains. Most grain boundaries are not clearly defined and are associated with a "mantle" region containing a higher density of dislocations. Few small grains in the nanometer scale (<100 nm) appear to be free of dislocations, corroborating reports of other researchers.[35,62] At higher magnification (Figure 4(b)),

better defined grain boundaries are observed from which dislocations are emitted. Moreover, dislocation arrays covering around 30 to 50 nm in the vicinity of the grain boundaries are observed. These arrays could be related to the dislocation activity at grain boundaries such as emission and bowing out. Figures 4(c) and (d) illustrate the microstructure of UFG Ti after compression at 293 K (20 °C) up to 0.2 pct plastic strain, at strain rates of 10^{-3} s^{-1} and 10^{-1} s^{-1}, respectively. The former lies in the hump with the DSA effect shown in Figure 2, whereas the latter is outside the hump, indicating that DSA was not triggered.

E. *Interstitial Diffusion Mechanism in UFG Ti*

Bulk diffusion is clearly too slow to enable DSA to occur in UFG Ti. Thus, a faster diffusion mechanism must be responsible for the appearance of room temperature DSA revealed in Figure 2. A mechanism is proposed in this section.

Grain boundaries are characterized by a higher concentration of lattice defects and a lower atomic density, rendering them favored sites for interstitials.[63] Interstitial segregation at grain boundaries is especially enhanced in SPD-produced UFG materials because grain boundary volume fraction is higher and stress-induced grain boundary segregation becomes significant.[64] Therefore, the concentrations of interstitials tend to be higher at grain boundaries than inside (middle) of the grain. Another characteristic of SPD-produced UFG materials is the non-equilibrated nature of grain boundaries owing to the higher densities of dislocations found in their vicinity.[65–67]

Figure 5 illustrates the proposed interstitial diffusion mechanism in UFG Ti. A grain with size d delineated by a grain boundary with thickness δ (colored in gray) undergoes plastic deformation. Dislocations emitted from grain boundaries bow-out into the grain interior. Segregated interstitials (N, O, C) at grain boundaries during the SPD processing flow along the dislocation cores, driven by the concentration gradient. The dashed lines in Figure 5 indicate the flux of interstitials with ongoing plastic deformation. The underlying physical principle of the proposed mechanism is that interstitials diffuse easily along dislocation cores and retard (drag) dislocation motion, eventually leading to DSA. The distribution of dislocations influences DSA in UFG Ti: the excessive dislocation density at grain boundaries, Figure 4, is crucial to the diffusion mechanism. The loose structure of grain boundaries, Figure 4(c), and the extended mantles lead to a fast path for interstitial diffusion. It should be noted that, according to Table I, oxygen with 3300 ppm in concentration is the strongest candidate for interstitial diffusion in UFG Ti, in comparison with nitrogen and carbon.

F. *Calculation of Dislocation Velocities*

In order to verify the proposed model, one has to compare the velocity of dislocations with that of interstitial flux. This can be accomplished through the

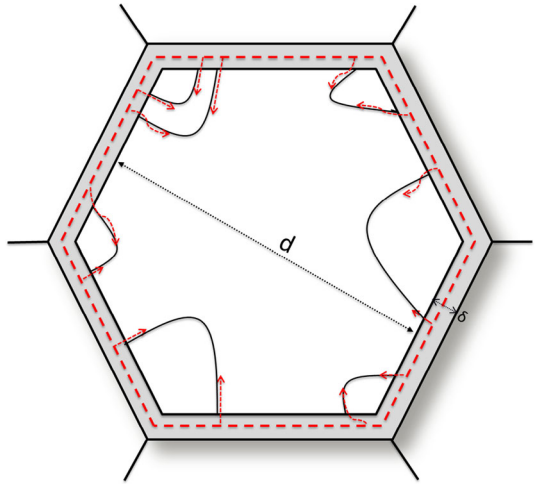

Fig. 5—Schematic representation of interstitial diffusion from the grain boundary (with characteristic thickness δ) and proceeding along the dislocation loops being emitted from the grain boundaries. Both advance of dislocation front and lateral expansion of loops are inhibited.

Orowan equation, which relates the shear strain γ to the mean free path (l) of dislocations:

$$\gamma = \rho_m b l, \qquad [6]$$

where ρ_m is the mobile dislocation density and b is the Burgers vector. By taking the time derivative and assuming that the dislocation generation rate does not affect the calculation, the shear strain rate, $\dot{\gamma}$, is

$$\dot{\gamma} = \rho_m b v \qquad [7]$$

The mobile dislocation velocity is v. For the same shear strain rate in both CG and UFG materials,

$$\rho_{m\_CG} \cdot b \cdot v_{CG} = \rho_{m\_UFG} \cdot b \cdot v_{UFG} \qquad [8]$$

and

$$\frac{v_{UFG}}{v_{CG}} = \frac{\rho_{m\_CG}}{\rho_{m\_UFG}} \qquad [9]$$

Two differences between CG and UFG are (a) the much greater concentration of dislocation sources at grain boundaries and (b) a lower dislocation mean free path for UFG Ti. If the concentration of grain boundary dislocation sources (θ) is proportional to the grain boundary surface per unit volume (S_V), then

$$\frac{\theta_{UFG}}{\theta_{CG}} = \frac{SV_{UFG}}{SV_{CG}} \qquad [10]$$

S_V, is topologically related to the grain size, d[58,68] by

$$S_V = \frac{3}{d} \qquad [11]$$

Thus,

$$\frac{\theta_{UFG}}{\theta_{CG}} = \frac{d_{CG}}{d_{UFG}} \quad [12]$$

Using $d_{CG} = 130\ \mu m$ and $d_{UFG} \approx 130$ nm as guiding parameters, the ratio θ_{UFG}/θ_{CG} is equal to 10^3. The mean free path for UFG Ti, l_{UFG}, can be considered as equal to the grain size, d_{UFG}. For the CG specimens, the mean free path is less than the grain size, since dislocations will have difficulty traversing entire grains. It is difficult to assess the mean free path of the dislocations, but the onset of plastic flow occurs primarily by their emission from the grain boundaries. Li[64] developed a model for grain size effect of flow stress based on the activation of grain boundary sources (ledges). In this case, the ratio of dislocation densities can be considered to be equal to that expressed in Eq. [12]. Thus, a factor of 10^3 can be assumed. Considering that an annealed CG material has $\rho_{f\_CG} \approx 10^{10}\ m^{-2}$, in the UFG Ti fabricated by SPD, ρ_{m_UFG} is roughly $10^{13}\ m^{-2}$. Applying Eq. [9], one obtains the ratio between dislocation velocities:

$$\frac{v_{CG}}{v_{UFG}} \approx 10^3 \quad [13]$$

Tanaka and Conrad[69] measured an edge dislocation velocity of 10^4 nm s^{-1} in CG titanium at an applied strain rate of 10^{-3} to $10^{-4}\ s^{-1}$. Substituting this value into Eq. [13] yields $v_{UFG} = 10$ nm/s. This lower dislocation velocity enables diffusion of interstitials along the dislocation core, resulting in enhanced pipe diffusion, as will be demonstrated in Section III–H.

G. *Validation of Diffusion Mechanism*

Kocks *et al.*[70] proposed that pipe diffusion is the physical mechanism responsible for DSA. Curtin *et al.*[71] also suggested diffusion by atomic jumps in the vicinity of dislocation core leads to the DSA in Al-Mg alloys. However, the activation energy Q_p for pipe diffusion in titanium is not available in the literature. Ishii *et al.*[72] simulated the interstitial pipe diffusion in bcc iron by molecular dynamics simulation. The results indicate a largely reduced activation energy for pipe diffusion, $\left(\frac{Q_p}{Q_B}\right)_{Fe} = \frac{1}{3}$.

It is possible to estimate the extent to which the interstitials diffuse during plastic deformation of UFG Ti, after the dislocations are generated from grain boundary sources, using standard diffusion equations. First, assume that all the interstitials have migrated to the grain boundaries prior to deformation (during ECAP and post ECAP period). Assuming a grain boundary thickness, $\delta \approx 4b = 2.3$ nm and idealized spherical grains, the volume fraction of grain boundary is

$$V_f \approx \frac{1}{2}\frac{4\pi R^2\delta}{\frac{4}{3}\pi R^3} = \frac{3\delta}{2R}, \quad [14]$$

where $4\pi R^2\delta$ is the approximate volume of the grain boundary regions. The $\frac{1}{2}$ term arises because the grain boundary is shared by two adjacent grains. For $R \approx 65$ nm, the grain boundary fraction is $V_f \approx 0.053$. The total concentration of interstitials, C_S, in the grain boundary is obtained by

$$C_S = \frac{C_B}{V_f}, \quad [15]$$

where $C_B \approx 0.01$ is the concentration, or atomic fraction, of interstitials in the bulk (only oxygen is considered since it has the highest concentration). Therefore, $C_S = 0.187$.

Assuming a constant concentration of C_S (infinite supply of interstitials at grain boundary) and that the diffusion of interstitials along the dislocations (pipe diffusion) is governed by the Dewey-Ostrand equation[73],

$$\frac{C(x,t) - C_s}{C_B - C_s} = \mathrm{erf}\left(\frac{x}{2\sqrt{D_p t}}\right), \quad [16]$$

where D_p is the pipe diffusion coefficient that is commonly taken as equal to the grain boundary diffusion coefficient:

$$D_p \approx D_{GB} = D_0 \exp\left(-\frac{Q_{GB}}{RT}\right) \quad [17]$$

Q_{GB} is the activation energy for grain boundary diffusion, usually considered to be between one-third and one-half of the bulk diffusion coefficient for high-angle grain boundary[72,74]:

$$Q_{GB} \approx 0.5\ Q_B \quad [18]$$

Considering that the pre-exponential factor D_0 is the same for pipe diffusion, grain boundary diffusion, and bulk diffusion, one can obtain D_p. Thus, for $Q_B \approx 170$ kJ/mol in CG Ti,[12,22] a value of $Q_{GB} \approx 85$ kJ/mol is obtained. It is not possible to justify the value of 17.3 kJ/mol found for UFG Ti at low temperatures from either Ishii *et al.*[72] calculation of one-third activation energy or Eq. [18] of one-half activation energy for pipe/grain boundary diffusion.

H. *Proposed New Mechanism*

The assumption is made that DSA manifests itself at the onset of plastic deformation. The time to plastically deforming the materials to a strain offset of $\varepsilon = 0.2$ pct at a strain rate of $10^{-3}s^{-1}$ is $t = \frac{\varepsilon}{\dot{\varepsilon}} = \frac{0.002}{10^{-3}s^{-1}} = 2$ s. Dislocation emission at grain boundaries by bow-out is considered the major source of plasticity. Figure 6(a) shows schematically the boundary and a dislocation loop being emitted from it. With the increase in time, a dislocation loop will advance into the grain interior. The displacement occurs only along x direction. Diffusion is faster in the vicinity of grain boundary, where a large concentration gradient exists, in contrast with the grain interior, where the concentration gradient drops sharply, as illustrated in (Figure 6(b)). The diffusion kinetics

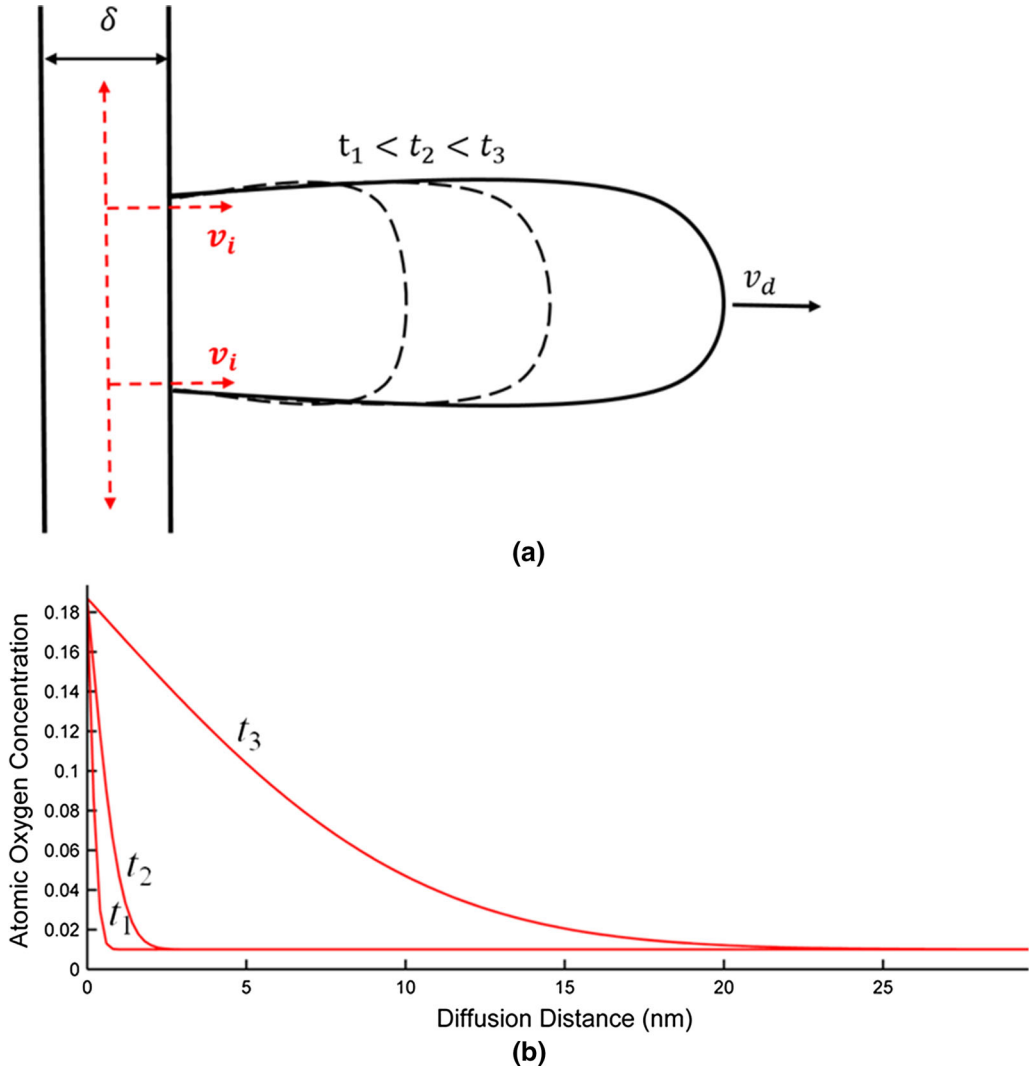

Fig. 6—(*a*) Schematic illustration of pipe diffusion in the vicinity of GB, and (*b*) calculated concentration profiles at 298 K (25 °C) and times, $t_1 = 0.2$ s, $t_2 = 2$ s and $t_3 = 200$ s. The time $t_2 = 2$ s is characteristic of a strain rate of 10^{-3} s^{-1}.

at a fixed distance from grain boundary, $x = 2$ nm, is evaluated below.

According to Fick's second law, concentration is a function of both diffusion time (t), and distance (x). Considering one as constant and the other as a variable, two different concentration profiles, C *vs* t and C *vs* x, can be obtained from Eq. [16]. The corresponding slopes of the two curves are $S_1 = \frac{dC}{dt}\big|_x$ and $S_2 = \frac{dC}{dx}\big|_t$. Dividing S_1 by S_2 gives

$$\frac{S_1}{S_2} = \frac{dC}{dt}\bigg|_x \times \frac{dx}{dC}\bigg|_t = \frac{dx}{dt}\bigg|_{t,x} \qquad [19]$$

The term $\frac{dx}{dt}\big|_{t,x}$ can be interpreted as the velocity of interstitial flux, $\bar{v}_i$, at a specific time and distance from grain boundary. As mentioned above, $t = 2$ s and $x = 2$ nm are of the greatest interest.

Figures 7(a) and (b) illustrate the concentration profiles with respect to time (at $x = 2$ nm) and distance ($t = 2$s), respectively. Taking the slopes from both curves gives, $S_1 = \frac{dC}{dt}\big|_{x=2\text{ nm}} = 2.85 \times 10^{-3}$ s^{-1}, $S_2 = \frac{dC}{dx}\big|_{t=2\text{ seconds}} = 0.011$ nm^{-1}. Therefore, $\bar{v}_i = \frac{dx}{dt}\big|_{t=2\text{ seconds}, x=2\text{nm}} = 0.26$ nm s^{-1}. This velocity will vary over a range of values for the regime that characterizes DSA. For instance, for a distance $x = 1$ nm, the velocity increases. However, the estimate at $t = 2$ seconds and $x = 2$ nm provides a good basis of comparison with the dislocation velocity estimated in Section III–F, $v_{\text{UFG}} = 10$ nm s^{-1}. The solute velocity is significantly lower than the dislocation velocity, but one should realize that these are first-order calculations with many approximations. Nevertheless, the predictions suggest that the interstitials can propagate a significant distance into dislocations as they emerge from the grain boundaries and can significantly alter their evolution, retarding their motion, and causing an attendant increase in the flow stress.

This explains the increased yield strength, Figure 2, of the UFG titanium in this range. As the dislocation loops expand, the concentration gradient drops and the

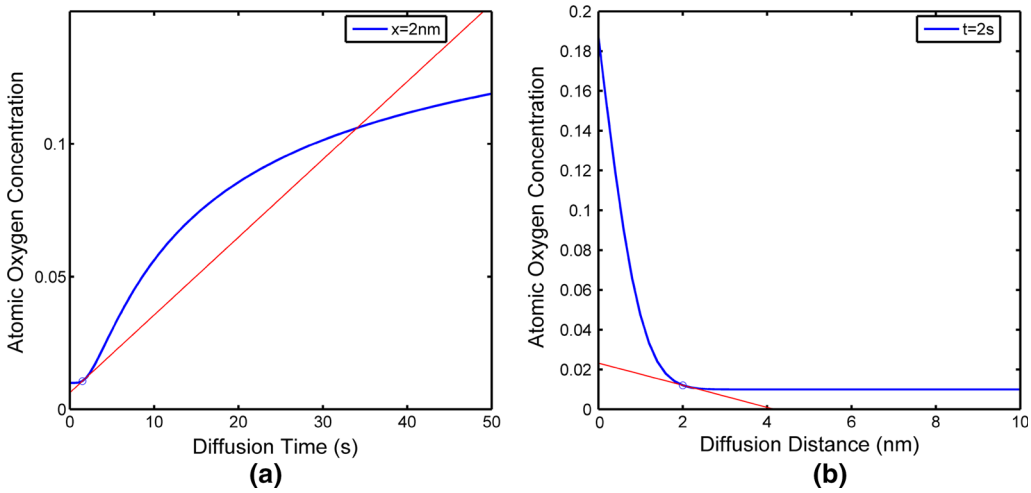

Fig. 7—(*a*) Interstitial concentration in the vicinity of GB as a function of diffusion time at fixed distance (2 nm), and (*b*) as a function of diffusion distance at fixed time ($t = 2$ s).

interstitial flux velocity correspondingly decreases, resulting in the breakaway of the dislocations. This can explain why no pronounced serrations are observed in the flow curves.

As a final remark, it is worth mentioning that a practical effect caused by the DSA at room temperature is the increment in strength, which may reach a value around 970 MPa, Figure 2, for a strain rate of 3×10^{-3} s^{-1}. This is higher than *RT* values reported for grades 2 and 4 ECAPed UFG Ti as well as CG Ti-6AL-4V alloy.[39] Because of the current use of UFG Ti in biomedical and dental applications,[46–52] which are restricted to room temperature, DSA may contribute to improved strength.

IV. SUMMARY AND CONCLUSIONS

- Ultrafine-gained titanium (UFG Ti) processed by ECAP-Conform was found to undergo DSA at the temperatures of 203 K (−70 °C), 293 K (20 °C) and 373 K (100 °C) under quasi-static compression tests in a strain rate range of 10^{-5} to 10^{-3} s^{-1}.
- Despite the absence of significant serrated flow in the stress–strain curves reported in UFG Ti at higher temperatures, DSA at lower temperatures was identified by anomalous high flow stress (compared with other alloyed titanium alloys), humps in the strain rate dependence of the yield stress, and negative strain rate sensitivity.
- A very low activation energy of 17.3 kJ/mol for DSA was calculated from the strain rate displacement of the stress humps with temperature. This could not be related to the bulk/pipe diffusion within the grain interior and therefore could not be accounted for RT temperature DSA in UFG Ti.
- A new mechanism for solute-dislocation interaction is proposed to explain the anomalous increase in the flow stress in the 10^{-3} to 10^{-4}s^{-1} strain rate range at ambient temperatures. Solute atoms, originating in the grain boundaries, diffuse along the dislocations being emitted from grain boundary sources and retard their advance. Based on Dewey-Ostrand's solution to the second Fick's law, the velocity of the interstitial flux, v_i, can be estimated. The calculation predicts that, at the onset of the plastic deformation, both v_i and v_d, the dislocation velocity, are on the order of nm/s, leading to the DSA at room temperature.

ACKNOWLEDGMENTS

The support by the Department of Energy under UC Labs Grant as well as by the Brazilian agencies CNPq, CAPES, and FAPERJ is acknowledged. Discussions with and guidance by Prof. H. Conrad are gratefully appreciated. Norm Olson provided valuable collaboration in TEM analyses. Prof. Z. Valiev generously provided the materials used in this investigation, which would not have been possible without his help.

REFERENCES

1. F.D. Rosi and E.C. Perkin: *ASM*, 1953, vol. 45, pp. 972–92.
2. W.R. Kiessel and M.J. Sinnott: *AIME*, 1953, vol. 197, pp. 331–338.
3. R.N. Orava, G. Stone, and H. Conrad: *Trans ASM*, 1966, vol. 59, pp. 171–84.
4. H. Conrad: *J. Phys.*, 1967, vol. 45, pp. 581–90.
5. N.G. Turner and W.T. Roberts: *J. Less-Common Met.*, 1968, vol. 16, pp. 37–44.
6. R.L. Jones and H. Conrad: *Scripta Metall.*, 1968, vol. 2, pp. 239–42.
7. S.N. Monteiro, A.T. Santhanam, and R.E. Reed-Hill: *The Science, Technology and Application of Titanium*, Pergamon Press, Oxford and New York, 1970, pp. 503–16.
8. A.T. Santhanam, V. Ramachandran, and R.E. Reed-Hill: *Metall. Trans.*, 1970, vol. 1, pp. 2593–98.

9. A.T. Santhanam and R.E. Reed-Hill: *Scripta Metall.*, 1970, vol. 4, pp. 529–31.
10. H. Conrad and R.L. Jones: *The Science, Technology and Application of Titanium*, Pergamon Press, Oxford and New York, 1970, pp. 489–501.
11. A.T. Santhanam and R.E. Reed-Hill: *Metall. Trans.*, 1971, vol. 2, pp. 2619–22.
12. A. Garde, A.T. Santhanam, and R.E. Reed-Hill: *Acta Metall.*, 1972, vol. 20, pp. 215–22.
13. M. Doner and H. Conrad: *Metall. Trans.*, 1973, vol. 4, pp. 2809–17.
14. S.N. Monteiro and R.E. Reed-Hill: *Metall. Trans.*, 1973, vol. 4, pp. 1011–15.
15. H. Conrad, M. Doner, and B. de Meester: *Titanium Science and Technology*, Plenum Press, New York, 1973, pp. 965–69.
16. K. Okazaki and H. Conrad: *Acta Metall.*, 1973, vol. 21, pp. 1117–29.
17. N.M. Madhava and R.W. Armstrong: *Metall. Trans.*, 1974, vol. 5, pp. 1517–19.
18. R.E. Reed-Hill: *Metall. Rev.*, 1974, vol. 2, pp. 218–40.
19. C. Yin, M. Döner, and H. Conrad: *Metall. Trans. A*, 1975, vol. 6, pp. 1901–08.
20. H. Conrad, B. de Meester, M. Doner, and K. Okazaki: Plenum Press, New York, 1975, pp. 1–45.
21. H. Sasano and H. Kimura In: *3rd International Conference on Titanium Alloys*, paper V-4, 1976; p. 117-126, Moscow.
22. H. Conrad: *Prog. Mater. Sci.*, 1981, vol. 26, pp. 123–403.
23. C.P. Venugopal, S. Venugopal, and V. Seetharaman: *J. Mater. Process. Tech.*, 1990, vol. 21, pp. 91–101.
24. S. Nemat-Nasser, W.G. Guo, and J.Y. Cheng: *Acta Mater.*, 1999, vol. 47, pp. 3705–20.
25. S.H. Chon, T.N. Kim, and J.K. Park: *Metals. Mater. Intl.*, 2004, vol. 10, pp. 567–73.
26. Y.H. Lin, K.H. Hu, F.H. Kao, S.H. Wang, J.R. Yang, and C.K. Lin: *Mater. Sci. Eng. A*, 2011, vol. 528, pp. 4381–89.
27. V.V. Stolyarov, Y.T. Zhu, T.C. Lowe, and R.Z. Valiev: *Mater. Sci. Eng., A*, 2001, vol. 303, pp. 82–89.
28. D. Jia, Y.M. Wang, K.T. Ramesh, E. Ma, Y.T. Zhu, and R.Z. Valiev: *Appl. Phys. Lett.*, 2001, vol. 79, pp. 611–13.
29. A.V. Sergueeva, V.V. Stolyarov, R.Z. Valiev, and A.K. Mukherjee: *Scripta Mater.*, 2001, vol. 45, pp. 747–52.
30. R.Z. Valiev, A.V. Sergueeva, and A.K. Mukherjee: *Scripta Mater.*, 2003, vol. 49, pp. 669–74.
31. V.V. Stolyarov, Y.T. Zhu, I.V. Alexandrov, and R.Z. Valiev: *Mater. Sci. Eng., A*, 2003, vol. 343, pp. 43–50.
32. X. Zao, W. Fu, X. Yang, and T.G. Langdon: *Scripta Mater.*, 2008, vol. 59, pp. 542–45.
33. I.P. Semenova, R.Z. Valiev, E.B. Yakushina, G.H. Salimgareeva, and T.C. Lowe: *J. Mater. Sci.*, 2008, vol. 43, pp. 7354–59.
34. G. Purcek, O. Saray, O. Kul, I. Karaman, G.G. Yapici, M. Haouaoui, and H.J. Maier: *Mater. Sci. Eng., A*, 2009, vol. 517, pp. 97–104.
35. X. Zhao, X. Yang, X. Liu, X. Wang, and T.G. Langdon: *Mater. Sci. Eng., A*, 2010, vol. 527, pp. 6335–39.
36. A.A. Mendes Filho, C.A. Rovere, S.E. Kuri, V.L. Sordi, and M. Ferrante: *Revista Materia.*, 2010, vol. 15, pp. 286–92.
37. G. Purcek, G.G. Yapici, I. Karaman, and H.J. Maier: *Mater. Sci. Eng., A*, 2011, vol. 528, pp. 2303–08.
38. I. Sabirov, M.T. Perez-Prado, J.M. Molina-Alderegia, I.P. Semenova, G.Kh. Salimgareeva, and R.Z. Valiev: *Scripta Mater.*, 2011, vol. 64, pp. 69–72.
39. Y. Zhang, R.B. Figueiredo, S.N. Alhajeri, J.T. Wang, N. Gao, and T.G. Langdon: *Mater. Sci. Eng., A*, 2011, vol. 528, pp. 7708–14.
40. V.L. Sordi, M. Ferrante, M. Kawasaki, and T.G. Langdon: *J. Mater. Sci.*, 2012, vol. 47, pp. 7870–76.
41. A.A. Mendes Filho, V.L. Sordi, and M. Ferrante: *Mater. Res.*, 2012, vol. 15, pp. 27–31.
42. W. Blum, Y.J. Li, and F. Breutinger: *Mater. Sci. Eng., A*, 2006, vol. 462, pp. 275–78.
43. Y.M. Wang, J.Y. Huang, T. Jiao, Y.T. Zhu, and A.V. Hamza: *J. Mater. Sci.*, 2007, vol. 42, pp. 1751–56.
44. X. Liu, X. Zhao, and X. Yang: *Mater. Sci. Forum*, 2011, vols. 667–669, pp. 707–12.
45. S.N. Monteiro, F.P.D. Lopes, E.A. Carvalho, and C.N. Elias: *J. Mater. Res. Technol.*, 2012, vol. 1, pp. 200–02.
46. V.V. Latysh, G. Krallics, I. Alexandrov, and I. Fodor: *Curr. Appl. Phys.*, 2006, vol. 6, pp. 262–66.
47. R.Z. Valiev, I.P. Semenova, V.V. Latysh, A.V. Shcherbakov, and E.B. Yakushina: *Nanotech. Russia.*, 2008, vol. 3, pp. 593–601.
48. R.Z. Valiev, I.P. Semenova, V.V. Latysh, H. Rack, T.C. Lowe, J. Petruželka, L. Dluhoš, D. Hrušák, and J. Sochová: *Adv. Eng. Mater.*, 2008, vol. vol. 10, pp. 15–B17.
49. J.W. Park, Y.J. Kim, C.H. Park, D.H. Lee, Y.G. Ko, J.H. Jang, and C.S. Lee: *Acta Mater.*, 2009, vol. 5, pp. 3272–80.
50. Y. Estrin, C. Kasper, S. Diederichs, and R. Lapovok: *J. Biomed. Mater. Res.*, 2009, vol. 90A, pp. 1239–42.
51. V.K. Truong, S. Rundell, R. Lapovok, Y. Estrin, J.Y. Wang, C.C. Berndt, D.G. Barnes, C.J. Fluke, R.J. Crawford, and E.P. Ivanova: *Appl. Microbiol. Biotech.*, 2009, vol. 83, pp. 925–37.
52. C.N. Elias, M.A. Meyers, R.Z. Valiev, and S.N. Monteiro: *J. Mater. Res. Technol.*, 2013, vol. 2, pp. 340–50.
53. C. Xu, S. Schroeder, P.B. Berbon, and T.G. Langdon: *Acta Mater.*, 2010, vol. 58, pp. 1379–86.
54. R.Z. Valiev and T.G. Langdon: *Metall. Mater. Trans. A*, 2011, vol. 42, pp. 2942–52.
55. American Society for Testing and Materials – ASTM International, Standard specification for titanium and titanium alloy bars and billets, B348-11, 2011.
56. American Society for Testing and Materials – ASTM International, Standard test methods for determination of hydrogen in titanium and titanium alloys by inert gas fusion thermal conductivity/infrared detection method, E1447-09, 2009.
57. American Society for Testing and Materials – ASTM International, Standard practice for microetching metals and alloys, E407-07, 2007.
58. J. Min, L.G. Hector, Jr, J. Lin, T. Jon Carter, and A.K. Sachdev: *Int. J. Plast.*, 2014, vol. 57, pp. 52–76.
59. A. Seeger: *Z. Naturforschung*, 1960, vol. 8, p. 128.
60. M.A. Meyers and K.K. Chawla: *Mechanical Behavior of Materials*, 2nd ed., Cambridge University Press, Cambridge, 2009, p. 497.
61. A.H. Cottrell: *Phil. Mag.*, 1953, vol. 44, pp. 829–32.
62. Y.T. Zhu, J.Y. Huang, J. Gubicza, T. Ungár, Y.M. Wang, E. Ma, and R.Z. Valiev: *J. Mater. Res.*, 2003, vol. 18, pp. 1908–17.
63. P. Lejcek: *Grain Boundary Segregation in Metals*, 1st ed., Springer, Berlin, 2010, p. 2.
64. J.C.M. Li: *Trans. TMS-AIME*, 1963, vol. 227, p. 239.
65. M.A. Meyers, A. Mishra, and D.J. Benson: *Prog. Mater Sci.*, 2006, vol. 51, pp. 427–556.
66. R.Z. Valiev and T.G. Langdon: *Prog. Mater Sci.*, 2006, vol. 51, pp. 881–981.
67. S. Zhao, C. Meng, F. Mao, W. Hu, and G. Gottstein: *Acta. Mater.* vol. 76. pp. 54–67.
68. R.T. De Hoff and F.N. Rhines: *Quantitative Microscopy*, McGraw-Hill, NY, 1968.
69. T. Tanaka and H. Conrad: *Acta Metall.*, 1971, vol. 19, pp. 1001–08.
70. A. Van Den Beukel and U.F. Kocks: *Acta Metallurgic.*, 1982, vol. 30, pp. 1027–34.
71. W.A. Curtin, D.L. Olmsted, and L.G. Hector: *Nat. Mater.*, 2006, vol. 5, pp. 875–80.
72. A. Ishii, J. Li, and S. Ogata: *PLoS One.*, 2013, vol. 8, p. e60586.
73. C.E. Van Orstrand and F.P. Dewey: "Preliminary Report on the Diffusion of Solids", USGS Professional Paper, 1915. pp. 83–96.
74. P.G. Shewmon: *Diffusion in solids*, 2nd ed., Wiley, Hoboken, 1989, p. 199.